

AN EFFICIENT BOUNDARY INTEGRAL EQUATION SOLUTION TECHNIQUE FOR SOLVING APERIODIC SCATTERING PROBLEMS FROM TWO-DIMENSIONAL, PERIODIC BOUNDARIES

R.FISHER¹, F. AGOCS², AND A. GILLMAN¹

ABSTRACT. This manuscript presents an efficient boundary integral equation technique for solving two-dimensional Helmholtz problems defined in the half-plane bounded by an infinite, periodic curve with Neumann boundary conditions and an aperiodic point source. The technique is designed for boundaries where one period does not require a large number of discretization points to achieve high accuracy. The Floquet–Bloch transform turns the problem into evaluating a contour integral where the integrand is the solution of quasiperiodic boundary value problems. To approximate the integral, one must solve a collection of these problems. This manuscript uses a variant of the periodizing scheme by Cho and Barnett which alleviates the need for evaluating the quasiperiodic Green’s function and is amenable to a large amount of precomputation that can be reused for all of the necessary solves. The solution technique is accelerated by the use of low rank linear algebra. The numerical results illustrate that the presented method is 20-30 faster than the technique utilizing the quasiperiodic Green’s function for a stair-like geometry.

1. INTRODUCTION

Periodic structures are commonly used in engineering applications to guide or localize electromagnetic and acoustic waves. They were first rigorously studied for the purposes of manufacturing and optimizing diffraction gratings [27], where they have been observed to give rise to modes that travel along the surface without attenuation. These guided (“trapped”) surface waves are defined as localized solutions of the wave equation without sources. They exist at a well-defined frequency, have finite energy, and are characterized by exponential decay in at least one direction. In the context of acoustic waves near periodic, open geometries, such as gratings, they are referred to as Rayleigh–Bloch surface waves, and have been studied extensively (see, e.g. [32, 30] and many references therein). Trapped modes have been exploited for filtering and sensing, such as decreasing the impact of water waves on off-shore structures [26, 19, 11], sound insulation or manipulation [25, 24], and in phononic and photonic crystals [20].

The existence of unattenuated surface waves, however, poses a challenge for numerical simulation, since truncation of the otherwise unbounded computational domain results in large reflections and numerical errors near the boundary. If the wave incident on the periodic boundary is quasiperiodic, i.e. periodic up to a complex phase, such as a plane wave, the solution is also expected to be quasiperiodic, and may therefore be periodized (computed over one unit cell of the periodic domain). In the case of an aperiodic incident field (e.g. the subject of this work, a cylindrical wave emanating from a line source), however, the solution does not possess any symmetry that may be exploited to make the computation tractable. Such aperiodic incident fields may still be considered via the Floquet–Bloch transform, a generalization of the Fourier transform, which decomposes them into quasiperiodic components. Each of the resulting fields defines a quasiperiodic scattering problem, parameterized

¹ DEPARTMENT OF APPLIED MATHEMATICS, UNIVERSITY OF COLORADO, BOULDER

² DEPARTMENT OF COMPUTER SCIENCE, UNIVERSITY OF COLORADO, BOULDER

by a Bloch phase. These individual problems may be solved by periodization. An integral of the quasiperiodic solutions over the Bloch phase then needs to be evaluated.

The Floquet–Bloch transform has been used to solve aperiodic scattering problems from 2D periodic arrays of Dirichlet obstacles [39, 8], continuous Neumann boundaries with corners [1], periodic closed waveguides [42], and locally perturbed periodic surfaces [41]. Three-dimensional, bi-periodic surfaces with Dirichlet or impedance boundary conditions have also been investigated [23, 3], where the Floquet–Bloch transform involves a nested integral.

Assuming time-harmonicity, the acoustic scattering process follows the two-dimensional Helmholtz equation in the upper half plane where the bottom boundary is defined by an infinite periodic curve Γ . Let Ω denote the domain where the partial differential equation is defined, as pictured in Figure 3.1(a). Throughout the manuscript, d denotes the length of one period of Γ . The Helmholtz problem for incident frequency ω and unknown total field $u_{\text{tot}}(\mathbf{x})$ is then

$$(1.1) \quad -(\Delta + \omega^2)u_{\text{tot}} = \delta(\mathbf{x} - \mathbf{x}_0) \quad \text{in } \Omega,$$

where \mathbf{x}_0 is the location of a point source. The boundary is a sound-hard surface resulting in Neumann boundary conditions

$$(1.2) \quad (u_{\text{tot}})_{\boldsymbol{\nu}} = \boldsymbol{\nu} \cdot \nabla u_{\text{tot}} = 0 \quad \text{on } \Gamma,$$

where $\boldsymbol{\nu}$ is the upwards-pointing unit normal vector for $\mathbf{x} \in \Gamma$. The total field is defined as $u_{\text{tot}} = u_i + u$ where u_i is a known incident wave generated by the point source at \mathbf{x}_0 and u is the scattered field defined as the solution to the boundary value problem

$$(1.3) \quad \begin{aligned} -(\Delta + \omega^2)u &= 0 && \text{in } \Omega, \\ u_{\boldsymbol{\nu}} &= -(u_i)_{\boldsymbol{\nu}} && \text{on } \Gamma, \end{aligned}$$

with a radiation condition in the y -direction.

By applying the Floquet–Bloch transform to (1.3), we find that the solution can be found by carrying out the Floquet–Bloch integral

$$(1.4) \quad u = \frac{d}{2\pi} \int_{-\frac{\pi}{d}}^{\frac{\pi}{d}} u_{\kappa} d\kappa,$$

where u_{κ} is the solution of

$$(1.5) \quad \begin{aligned} -(\Delta + \omega^2)u_{\kappa} &= 0 && \text{in } \Omega, \\ (u_{\kappa})_{\boldsymbol{\nu}} &= -f_{\boldsymbol{\nu}} && \text{on } \Gamma. \end{aligned}$$

$f_{\boldsymbol{\nu}}$ is the normal derivative of the incident field generated by a quasiperiodic array of point sources,

$$(1.6) \quad f(\mathbf{x}) = \sum_{l \in \mathbb{Z}} \alpha^l H_0^{(1)}(\omega|\mathbf{x} - \mathbf{x}_0 - l\mathbf{d}|),$$

with $\mathbf{d} = (d, 0)$. The parameter $\alpha = e^{i\kappa d}$ denotes the Bloch phase. The radiation condition in the y direction can be defined via a Rayleigh–Bloch expansion. This is a Fourier series with discrete horizontal and vertical wavenumbers defined by

$$(1.7) \quad u_{\kappa} = \sum_{m \in \mathbb{Z}} b_m e^{i(\beta_m x + k_m y)},$$

where

$$(1.8) \quad \begin{aligned} \beta_m &= \kappa + 2\pi m/d, \\ k_m &= \begin{cases} \sqrt{\omega^2 - \beta_m^2} & \text{if } \omega \geq |\beta_m|, \\ i\sqrt{\beta_m^2 - \omega^2} & \text{otherwise,} \end{cases} \end{aligned}$$

for $m \in \mathbb{Z}$ and b_m are the expansion coefficients. The solution u_κ to this half-space boundary value problem satisfies the following quasiperiodic condition:

$$(1.9) \quad u_\kappa(x, y) = \alpha^{-1} u_\kappa(x, y + d)$$

Algorithm 1 provides a high level view of the proposed solution technique for evaluating the integral (1.4).

There are a variety of methods for approximating solutions to the quasiperiodic scattering problem (1.5). For the purposes of this manuscript, we will focus on methods designed for recasting (1.3) as an integral equation. A commonly used approach is to use the quasiperiodic Green's function [12, 7, 31, 28, 1]. The main challenges with this approach are that the quasiperiodic Green's function is defined as an infinite sum that can be slowly convergent, and is not convergent at Wood's anomalies. There exist fast algorithm techniques for handling the infinite sum, many of which are reviewed in [29]. Another drawback of using the quasiperiodic Green's function approach is that it needs to be recomputed for each Bloch phase α . One example is [1], which uses the lattice sum approach from [40] to compute the quasiperiodic Green's function. It then defines and solves a new integral equation at each Bloch phase involved in the Floquet–Bloch transform, recomputing all matrices each time. Due to the breakdown of the lattice sum approach, the Floquet–Bloch integral involved needs to avoid Bloch phases where Wood's anomalies occur.

An alternative approach for quasiperiodic scattering problems that avoids the use of the quasiperiodic Green's function was first presented in [4]. It was further generalized in [10]. The idea is to represent the solution via integral operators that involve the free space Green's function plus and additional basis functions whose coefficients are unknown. The unknowns are found by solving a system found by enforcing the boundary condition and quasiperiodicity. The main advantages to this approach are that 1) it is robust at Wood's anomalies, and 2) the system can be broken up into Bloch phase-dependent and independent pieces. This allows a significant portion of a direct solver to be precomputed and used for all solves independent of the Bloch phase. In [13], exploiting this precomputation led to a 600 times speedup over solving the same linear system using an FMM-accelerated GMRES solver for a problem involving over 200 right-hand-sides. The ideas in [13] have been extended to multilayered media scattering problems involving periodic interfaces [43, 44, 38]. These fast solvers are only necessary if the number of discretization points needed to resolve one period of the boundary is large.

For the problems of interest in this manuscript, not many points are needed to discretize the boundary and obtain accurate approximate solutions to equation (1.3). Thus we choose to use the periodizing method presented in [10] modified for a Neumann boundary condition on the interface. We created a new efficient direct solver that is inspired by the methods in [13, 43, 44] for the linear system that results from the discretization of the integral equation. This solver is specifically designed for problems where the system is not large enough to justify the use of the fast direct solvers from [13, 43, 44]. For the systems under consideration, the solver has a relatively lean precomputation, reuses information that is independent of the Bloch phase, and can be applied very fast for the multiple solves needed in the Floquet–Bloch integral.

ALGORITHM 1: High level algorithm

Given an aperiodic point source at location \mathbf{x}_0 and two-dimensional periodic boundary Γ , approximate $u = \frac{d}{2\pi} \int_{-\pi/d}^{\pi/d} u_\kappa d\kappa$.

Create N_κ quadrature nodes $\{\kappa_j\}$ and weights $\{w_j\}$ on the contour curve $\kappa(s)$ defined in (2.2).

Pre-compute the α -independent portions of the Helmholtz direct solver as defined in section 4.

loop over all κ_j ,

 Create the boundary data for κ_j via the method in section 3.4.

 Solve a quasiperiodic scattering problem to find u_{κ_j} using the algorithm presented in Section 4.

end loop

Evaluate $u = \frac{d}{2\pi} \sum_{j=1}^{N_\kappa} w_j u_{\kappa_j}$.

The goal of this manuscript is to illustrate how several numerical methods—including the Floquet–Bloch approach, a boundary integral equation method, an associated fast solver, and the recycling of matrices involved—may be combined to significantly reduce the computation time needed to solve aperiodic scattering problems in periodic geometries, by pushing more of the computational effort into operations carried out once at the start of the process. In three dimensional, biperiodic structures, the inverse Floquet–Bloch transform becomes a nested integral, requiring an even larger number of quasiperiodic solves. Each solve involves a three-dimensional periodic surface, which increases the system size. Putting the bulk of the computational cost into a precomputation step will therefore become crucial for developing a computationally viable method.

The manuscript proceeds by first introducing the Floquet–Bloch integral in section 2. The boundary integral periodization technique is presented in section 3. This section also includes a technique for representing a quasiperiodic array of point charges via the free-space Helmholtz Green’s function. Section 4 presents the proposed efficient direct solver technique including a method of handling boundaries with corners. Section 5 illustrates the performance of the proposed solver for solving the boundary value problem in (1.3) and computing the Floquet–Bloch integral. Section 6 closes the document with a summary and a discussion the goal of extending this technique to three-dimensional problems.

2. FLOQUET–BLOCH INTEGRAL

A common way of making the aperiodic problem tractable is to represent the scattered solution u as an integral of quasiperiodic solutions via the Floquet–Bloch transform. The transform utilizes the identity

$$\begin{aligned}
 \delta(\mathbf{x} - \mathbf{x}_0) &= \frac{d}{2\pi} \int_{-\frac{\pi}{d}}^{\frac{\pi}{d}} \sum_{n \in \mathbb{Z}} \delta(\mathbf{x} - \mathbf{x}_0 - n\mathbf{d}) e^{in\kappa d} d\kappa \\
 &= \frac{d}{2\pi} \int_{-\frac{\pi}{d}}^{\frac{\pi}{d}} \sum_{n \in \mathbb{Z}} \delta(\mathbf{x} - \mathbf{x}_0 - n\mathbf{d}) \alpha^n d\kappa.
 \end{aligned}
 \tag{2.1}$$

The left-hand-side of (2.1) is the common representation of a point source (delta function). The integrand on the right-hand-side of (2.1) is an infinite, quasiperiodic array of point sources with an associated constant phase difference α from section 1.

By linearity, it follows that the aperiodic scattered solution u to equation (1.3) may be written as the integral in equation (1.4), and that u_κ satisfies equation (1.5). The quasiperiodic scattered solution u_κ is unique at all values of $\kappa \in [-\pi/d, \pi/d]$, except potentially a discrete set [6]. These values of κ correspond to on-surface wavenumbers of trapped modes, which do not decay in the horizontal direction but decay exponentially in the vertical direction.

A further consequence of quasiperiodicity is that on-surface wavenumbers are only unique modulo $2\pi/d$, since κ and $\beta_n := \kappa + 2n\pi/d$ for $n \in \mathbb{Z}$ give the same Bloch phase α . For an incident frequency ω and real on-surface wavenumber β_n , the vertical wavenumber k_n is then either positive real or positive imaginary, as given by (1.8). Physically, having k_n be purely real means the vertical component of the solution is a propagating (outgoing) wave, whereas it decays exponentially for a purely imaginary k_n . The $k_n = 0$ case, where the behavior of the vertical component of the scattered field abruptly changes, corresponds to a Wood anomaly [37].

Figure 2.1 is a sketch of the integrand u_κ of the Floquet–Bloch transform in the complex κ -plane. We denote the values of κ that correspond to trapped modes by κ_{tr} . The values κ_{tr} present as poles, whereas the Wood anomalies can be shown to be $z^{-1/2}$ -type singularities [4], both on the real axis. There are branch cuts emanating from the Wood anomalies, the directions and shapes of which are determined by how k_n is evaluated for a general complex-valued κ (and β_n). In this work, the choice in (1.8) leads to branch cuts that are circular arcs, and together with the choice of integration contour for the Floquet–Bloch integral ensures that the solution is outgoing.

In order to evaluate the integral in equation (1.4), we define a contour parameterized by $s = \Re(\kappa)$ that avoids the branch cuts and the Wood anomalies. In Figure 2.1 and our numerical examples, the parameterization is given by

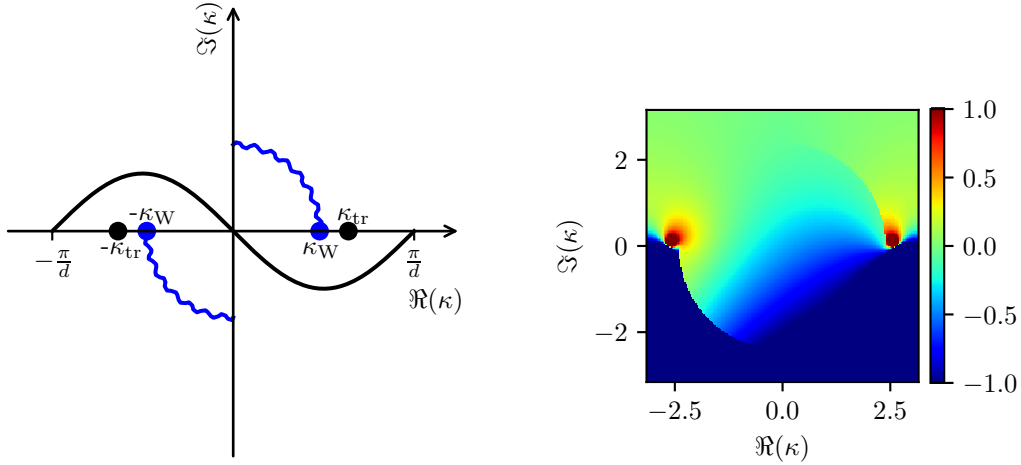
$$(2.2) \quad \kappa(s) = s - i \sin(sd), \quad s \in \left[-\frac{\pi}{d}, \frac{\pi}{d} \right).$$

For the examples under consideration, the amplitude of this sinusoidal contour has previously been set by convergence testing in Figure 9 of [1].

To approximate the integral in equation (1.4), a collection of quadrature points are placed on $\kappa(s)$. Since the integrand is periodic (the points $\kappa = \pm\pi/d$ are equivalent), the periodic trapezoidal rule is quickly convergent [36]. However, in the limits $\omega \rightarrow 0$ and $\omega \rightarrow \omega_c$, where ω_c is the largest frequency at which trapped modes exist, the integration contour $\kappa(s)$ passes between two poles coalescing at $\kappa_{\text{tr}} = 0$ and $\kappa_{\text{tr}} = \pm\pi/d$, respectively. In these cases, we increase the density of quadrature nodes in the vicinity of the coalescing poles according to [5, 1]. The method works by taking quadrature nodes that are evenly spaced in s along the path (2.2), and modifying their density to $\theta(s)$, a function numerically computed from its derivative that takes its maximum near the point(s) where bunching is required. The function $\theta(s)$ is defined as

$$(2.3) \quad \kappa(s) = \theta(s) - i \sin(\theta(s)), \quad \theta'(s) = \begin{cases} \alpha \cosh(b \sin \frac{sd}{2}) & \text{when } \kappa_{\text{tr}} \rightarrow \pi/d, \\ \alpha \cosh(b \sin \frac{sd-\pi}{2}) & \text{when } \kappa_{\text{tr}} \rightarrow 0 \end{cases}$$

where b is a free parameter, the normalization parameter α is obtained from the requirement that $\int_0^{2\pi/d} \theta'(s) ds = 2\pi/d$, and $\theta(s)$ is computed from $\theta'(s)$ by taking the antiderivative of its spectral interpolant using the FFT. Using (2.3) results in nodes that are evenly spaced



(A) Sketch of the Floquet–Bloch integration contour, with branch cuts and poles labeled. (B) Real part of the integrand of the inverse Floquet–Bloch transform.

FIGURE 2.1. Deformation of the integral contour for the Floquet–Bloch transform. (a) The black, sinusoidal curve shows the deformed contour that goes around the poles corresponding to trapped modes (κ_{tr} , black dots) and branch cuts corresponding to Wood anomalies (κ_W , blue dots and wavy lines). (b) Shows the real part of the integrand u_κ in the inverse Floquet–Bloch transform (1.4), with the branch cuts and poles visible, evaluated at the target point $\mathbf{x} = [0.22, 0.34]$, with $\omega = 2.4$.

in s being mapped to be a factor e^b closer together near $\kappa_{tr} \in \{0, \pm\pi/d\}$. The value of b can be adjusted as needed.

Each quadrature location requires solving one quasiperiodic scattering problem with the same wave speed but different Bloch phase α and boundary condition. Thus it is necessary to have an efficient numerical method for approximating the value u_κ .

3. THE PERIODIZING SCHEME

The periodization scheme used in this manuscript is a variation of the method presented in [10] that has been modified for an interface with Neumann boundary conditions. The method in [10] can be viewed as a modified version of the integral formulation in [22, 33]. The presentation of the periodization scheme is kept relatively brief. Detailed explanations are available in [10, 43, 44].

This section breaks the periodization scheme into three pieces: the partitioning of the domain, the representation of the solution to the Neumann problem, and the linear system that must be solved. Section 4 presents the proposed technique for solving the linear system. Section 3.4 presents the application of the periodization technique for representing a quasiperiodic array of point charges.

3.1. Partitioning of the geometry. The periodization scheme begins by partitioning the domain Ω and introducing the idea of a *unit cell*. The unit cell is a rectangle where the left and right boundaries are defined to bound one copy of periodic surface. The top boundary is placed above at some location not close to the periodic surface. The bottom boundary can lie anywhere below the periodic surface. Figure 3.1(b) illustrates the unit cell. Let $x = x_L$ and $x = x_R$ denote the left and right bounds of the unit cell. Let $y = y_U$

denote the upper bound of the unit cell. For the Neumann boundary value problem, the interface surface is the lower bound of the unit cell. Let Γ_0 denote the portion of the lower boundary inside the unit cell. Similarly, Γ_{-1} and Γ_1 denote the portions of the lower boundary corresponding to the left and right periods of Γ_0 , respectively.

3.2. Representation of the solution. Within the unit cell, the solution is represented via a linear combination of an integral formulation using the two-dimensional free-space Green function $G_\omega(\mathbf{x}, \mathbf{y}) = \frac{i}{4} H_0^{(1)}(\omega \|\mathbf{x} - \mathbf{y}\|)$ and an additional contribution to enforce quasiperiodicity. The additional contribution is given by a linear combination of basis functions created by proxy charges placed at a collection of N_{proxy} points on a circle \mathcal{P} of radius $R_{\text{proxy}} \in [\frac{3d}{2}, 2d]$ [10]. Each point \mathbf{y}_j on the proxy surface \mathcal{P} has a corresponding proxy basis function $\phi_j(\mathbf{x})$ defined by

$$(3.1) \quad \phi_j(\mathbf{x}) = \frac{\partial G_\omega}{\partial \nu_j}(\mathbf{x}, \mathbf{y}_j) + i\omega G_\omega(\mathbf{x}, \mathbf{y}_j),$$

where ν_j is the outward-pointing normal vector at \mathbf{y}_j .

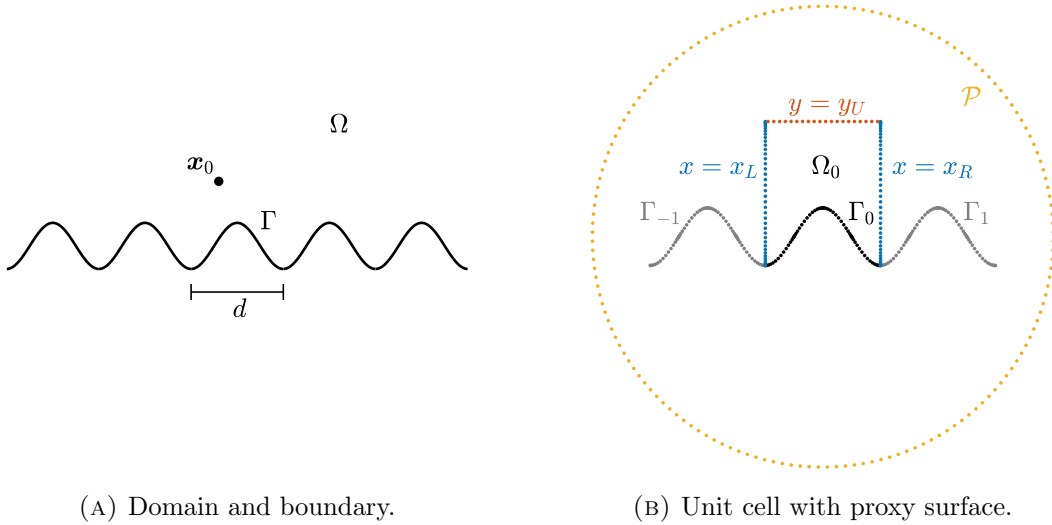


FIGURE 3.1. Illustration of the (a) geometry and the (b) unit cell. (a) A portion of the domain Ω and boundary Γ are shown for the cosine geometry. The point source \mathbf{x}_0 and the periodicity d are labeled. (b) The unit cell is shown with its boundary Γ_0 in black, left and right walls in blue, and upper wall in red. The unit cell domain Ω_0 is labeled. The left and right neighbors, Γ_{-1} and Γ_1 , are shown in gray. The proxy circle \mathcal{P} with charges $\{y_j\}_{j=1}^{N_{\text{proxy}}}$ is shown in orange encompassing the unit cell and its two neighbors.

Specifically, the solution in the unit cell is expressed as

$$(3.2) \quad u(\mathbf{x}) = (\tilde{\mathcal{S}}_\Gamma \sigma)(\mathbf{x}) + \sum_{j=1}^{N_{\text{proxy}}} c_j \phi_j(\mathbf{x}),$$

where

$$(3.3) \quad (\tilde{\mathcal{S}}_\Gamma \sigma)(\mathbf{x}) = \sum_{l=-1}^1 \alpha^l \int_{\Gamma_0} G_\omega(\mathbf{x}, \mathbf{y} + l\mathbf{d}) \sigma(\mathbf{y}) ds(\mathbf{y}).$$

Note that the kernel of $(\tilde{\mathcal{S}}_\Gamma \sigma)$ includes contributions from the left (Γ_{-1}) and right (Γ_1) copies of the unit cell boundary, appropriately scaled by the Bloch phase α , in addition to the contribution from the boundary Γ_0 included in the unit cell. The boundary charge density σ and the coefficients for the proxy charges $\{c_j\}_{j=1}^{N_{\text{proxy}}}$ are yet to be determined.

Above the unit cell (i.e. for points in the unit strip where $y > y_U$), the solution is given by a Rayleigh–Bloch expansion. This expansion is uniformly convergent [6] and satisfies the radiation condition. Specifically, for $\mathbf{x} = (x, y)$ in the unit strip where $y > y_U$, the solution is given by

$$(3.4) \quad u(x, y) = \sum_{n \in \mathbb{Z}} a_n e^{i\beta_n x} e^{ik_n(y-y_U)}$$

where β_n and k_n are the on-surface and vertical wavenumbers as defined in (1.8), and the set $\{a_n\}$ are coefficients to be determined.

3.3. The linear system. The representations inside and outside the unit cell satisfy the partial differential equation in their respective regions, but they do not naturally enforce the boundary condition, quasiperiodicity of the solution, or continuity of the representations through the line $y = y_U$. Enforcing these conditions provides equations that can be solved to find the three sets of unknowns: $\sigma(x)$, $\{c_j\}_{j=1}^{N_{\text{proxy}}}$, and $\{a_n\}$.

The following boundary integral equation results from enforcing the Neumann boundary condition on Γ_0 :

$$(3.5) \quad -\frac{1}{2}\sigma(\mathbf{x}) + (\tilde{\mathcal{D}}_{\Gamma_0}^* \sigma)(\mathbf{x}) + \sum_{j=1}^{N_{\text{proxy}}} c_j \partial_{\nu_{\mathbf{x}}} \phi_j(\mathbf{x}) = g(\mathbf{x}) \quad \text{for } \mathbf{x} \in \Gamma_0,$$

where

$$(3.6) \quad (\tilde{\mathcal{D}}_{\Gamma_0}^* \sigma)(\mathbf{x}) = \sum_{l=-1}^1 \alpha^l \int_{\Gamma_0} \partial_{\nu_{\mathbf{x}}} G_\omega(\mathbf{x}, \mathbf{y} + l\mathbf{d}) \sigma(\mathbf{y}) ds(\mathbf{y})$$

is the adjoint double layer kernel and $g(\mathbf{x}) = -f_\nu(\mathbf{x})$ from (1.6).

The next equation enforces quasiperiodicity of the solution,

$$(3.7) \quad \left((\tilde{\mathcal{S}}_{\Gamma_0} \sigma)(\mathbf{x}) + \sum_{j=1}^{N_{\text{proxy}}} c_j \phi_j(\mathbf{x}) \right) \Big|_{x=x_L} = \alpha^{-1} \left((\tilde{\mathcal{S}}_{\Gamma_0} \sigma)(\mathbf{x}) + \sum_{j=1}^{N_{\text{proxy}}} c_j \phi_j(\mathbf{x}) \right) \Big|_{x=x_R}.$$

The equation for enforcing continuity of the flux is

$$(3.8) \quad \left((\tilde{\mathcal{D}}_\Gamma^* \sigma)(\mathbf{x}) + \sum_{j=1}^{N_{\text{proxy}}} c_j \partial_{\nu_{\mathbf{x}}} \phi_j(\mathbf{x}) \right) \Big|_{x=x_L} = \alpha^{-1} \left((\tilde{\mathcal{D}}_\Gamma^* \sigma)(\mathbf{x}) + \sum_{j=1}^{N_{\text{proxy}}} c_j \partial_{\nu_{\mathbf{x}}} \phi_j(\mathbf{x}) \right) \Big|_{x=x_R}.$$

The last set of equations enforce continuity of the two representations and their derivatives through the top of the unit cell. The equations are given by

$$(3.9) \quad \left((\tilde{\mathcal{S}}_\Gamma \sigma)(\mathbf{x}) + \sum_{j=1}^{N_{\text{proxy}}} c_j \phi_j(\mathbf{x}) \right) \Big|_{y=y_U} = \left(\sum_{n \in \mathbb{Z}} a_n e^{i\kappa_n x} e^{ik_n(y-y_U)} \right) \Big|_{y=y_U},$$

$$(3.10) \quad \left((\tilde{\mathcal{D}}_\Gamma^* \sigma)(\mathbf{x}) + \sum_{j=1}^{N_{\text{proxy}}} c_j \partial_{\nu_{\mathbf{x}}} \phi_j(\mathbf{x}) \right) \Big|_{y=y_U} = \left(\sum_{n \in \mathbb{Z}} a_n i\beta_n e^{i\beta_n x} e^{ik_n(y-y_U)} \right) \Big|_{y=y_U}.$$

Equations (3.5–3.10) are continuous equations that cannot be solved directly; their solution needs to be approximated. We choose to approximate the integral operators via a Nyström discretization. Let $\{\mathbf{x}_j\}_{j=1}^N$ denote the quadrature nodes on Γ_0 used in the Nyström discretization. In the same manner as [10], the quasiperiodicity of the solution and its flux are enforced at points that lie on Gaussian panels on the left and right walls of the unit cell. Let M_w denote the number of points used to enforce quasiperiodicity. Lastly, the continuity of the integral representation and the Rayleigh–Bloch expansions is enforced at collection of M uniformly distributed points on the top of the unit cell. The Rayleigh-Bloch expansion is truncated at $n = \pm K$.

The rectangular linear system that arises from these choices has the form

$$(3.11) \quad \begin{bmatrix} \mathbf{A} & \mathbf{B} & \mathbf{0} \\ \mathbf{C} & \mathbf{Q} & \mathbf{0} \\ \mathbf{Z} & \mathbf{V} & \mathbf{W} \end{bmatrix} \begin{bmatrix} \boldsymbol{\sigma} \\ \mathbf{c} \\ \mathbf{a} \end{bmatrix} = \begin{bmatrix} \mathbf{g} \\ \mathbf{0} \\ \mathbf{0} \end{bmatrix}$$

where \mathbf{A} is a matrix of size $N \times N$, \mathbf{B} is a matrix of size $N \times N_{\text{proxy}}$, \mathbf{C} is a matrix of size $M_w \times N$, \mathbf{Q} is a matrix of size $M_w \times N_{\text{proxy}}$, \mathbf{Z} is a matrix of size $2M \times N$, \mathbf{V} is a matrix of size $2M \times N_{\text{proxy}}$, and \mathbf{W} is a matrix of size $2M \times 2K + 1$. The first block row equation enforces the Neumann boundary condition. The second block row equation enforces the quasiperiodicity of the solution and the flux. The last block row equation enforces continuity of the integral representation and the Rayleigh–Bloch expansions. Details on the specifics of the matrix entries are provided in [10, 43, 44].

3.4. Representing a quasiperiodic point source. Recall that the boundary data f_ν in the differential equation (1.5) is the normal derivative of a quasiperiodic point source evaluated on the boundary Γ . The periodizing scheme from earlier in this section can be used to create the quasiperiodic point source. The normal derivative of it can be used to evaluate f_ν .

Let $\hat{\mathbf{x}}$ denote the location of a point source located in the unit cell. Then for \mathbf{x} inside the unit cell, the effect of the point source $\psi(\mathbf{x}, \hat{\mathbf{x}})$ is given by

$$(3.12) \quad \psi(\mathbf{x}, \hat{\mathbf{x}}) = \sum_{l=-1}^1 \alpha^l G_\omega(\mathbf{x}, \hat{\mathbf{x}}) + \sum_{j=1}^P \hat{c}_j \phi_j(\mathbf{x})$$

Above the unit cell, the field is given by a Rayleigh–Bloch expansion as seen in equation (3.4). Let $\{\hat{a}_n\}$ denote the coefficients of this expansion.

With these representations, it is possible to follow the example from the previous subsection to create a linear system. The big difference is that there is no integral operator and no boundary condition to satisfy. In other words, the system looks similar to (3.11) except the first block row equation does not exist. The resulting linear system is given by

$$(3.13) \quad \begin{bmatrix} \mathbf{Q} & \mathbf{0} \\ \mathbf{V} & \mathbf{W} \end{bmatrix} \begin{bmatrix} \hat{\mathbf{c}} \\ \hat{\mathbf{a}} \end{bmatrix} = - \begin{bmatrix} \mathbf{C} \\ \mathbf{Z} \end{bmatrix}.$$

Here the matrices \mathbf{C} and \mathbf{Z} are the evaluation of $\sum_{l=-1}^1 \alpha^l G_\omega(\mathbf{x}, \hat{\mathbf{x}})$ and its flux on the left/right walls and the top of the unit cell, respectively. The other matrices are as defined in the last section. In practice, the linear system in equation (3.13) is small and can quickly be solved using a backward stable application of the pseudoinverse.

4. EFFICIENT DIRECT SOLUTION TECHNIQUE

For each quadrature node κ for approximating the integral (1.4), the linear system (3.11) must be solved. As long as the number of points N on the boundary is not large, it is possible to solve the system for each κ via dense linear algebra. When N is large (i.e. $N > 10,000$ depending on computational resources), it is possible to build a fast direct solver similar to the ones presented in [43, 13, 44]. This class of fast solvers is not necessary for the geometries of interest in this paper since they do not require a large number of discretization points. This section presents the proposed solution technique that utilizes some ideas from [43, 13, 44] coupled with other acceleration techniques that are ideal for the matrix sizes under consideration.

Algorithm 2 provides an overview of the precomputation steps in the solution technique.

The proposed direct solver is based on the creation of a block solve for the linear system (3.11). We choose to solve this system in a block-solve format;

$$(4.1) \quad \begin{aligned} \mathbf{b} &= \mathbf{S}^\dagger \hat{\mathbf{C}} \mathbf{A}^{-1} \mathbf{g}, \\ \boldsymbol{\sigma} &= \mathbf{A}^{-1} \mathbf{g} - \mathbf{A}^{-1} \hat{\mathbf{B}} \mathbf{b}, \end{aligned}$$

where $\mathbf{b} = \begin{bmatrix} \mathbf{c} \\ \mathbf{a} \end{bmatrix}$, $\hat{\mathbf{Q}} = \begin{bmatrix} \mathbf{Q} & \mathbf{0} \\ \mathbf{V} & \mathbf{W} \end{bmatrix}$, $\hat{\mathbf{C}} = \begin{bmatrix} \mathbf{C} \\ \mathbf{Z} \end{bmatrix}$, $\hat{\mathbf{B}} = [\mathbf{B} \ \mathbf{0}]$, and

$$(4.2) \quad \mathbf{S} = \hat{\mathbf{Q}} - \hat{\mathbf{C}} \mathbf{A}^{-1} \hat{\mathbf{B}}$$

denotes the Schur complement of the block system. The matrix \mathbf{S}^\dagger denotes the pseudoinverse of \mathbf{S} .

It is necessary to reuse as much computation as possible in order to create an efficient direct solver. The first place for computational savings is in the evaluation of the linear system. Specifically, the entries of all the matrices except for \mathbf{W} are made up of linear combinations of the same matrices, just scaled appropriately by the Bloch phase α . Thus all the unscaled matrices can be precomputed.

The next place for acceleration is in the inversion of \mathbf{A} which must be done for each Bloch phase α . The matrix \mathbf{A} can be written as

$$\mathbf{A} = \mathbf{A}_0 + \alpha \mathbf{A}_1 + \alpha^{-1} \mathbf{A}_{-1},$$

where \mathbf{A}_0 denotes the contribution due to the unit cell acting on itself, and \mathbf{A}_{-1} and \mathbf{A}_1 denote the contributions from the left and right neighbor geometries Γ interacting with the unit cell, respectively. These correspond to $l = 0, -1$, and 1 in the sum of the integral operators (3.6).

The matrices \mathbf{A}_{-1} and \mathbf{A}_1 are low-rank because they predominately correspond to interaction of points that are far from each other. Let $\mathbf{L}_{-1} \mathbf{R}_{-1}$ and $\mathbf{L}_1 \mathbf{R}_1$ denote the low-rank factorizations of \mathbf{A}_{-1} and \mathbf{A}_1 , respectively. Section 4.1 presents the technique for creating the low-rank factorizations. Let $\mathbf{L} = [\mathbf{L}_{-1} \ \mathbf{L}_1]$ and $\mathbf{R} = \begin{bmatrix} \alpha^{-1} \mathbf{R}_{-1} \\ \alpha \mathbf{R}_1 \end{bmatrix}$. Then the inverse of \mathbf{A} can be approximated using these factorization and the Woodbury formula,

$$(4.3) \quad \mathbf{A}^{-1} \approx (\mathbf{A}_0 + \mathbf{L} \mathbf{R})^{-1} = \mathbf{A}_0^{-1} - \mathbf{A}_0^{-1} \mathbf{L} (\mathbf{I} + \mathbf{R} \mathbf{A}_0^{-1} \mathbf{L})^{-1} \mathbf{R} \mathbf{A}_0^{-1}.$$

Note that the inverse \mathbf{A}_0^{-1} can be created once and used for all α . For each α , the sub-blocks of \mathbf{R} only need to be scaled accordingly. In practice, the matrix in (4.3) is never created. Instead it is applied rapidly to any vector \mathbf{f} using the formula

$$(4.4) \quad (\mathbf{A}_0 + \mathbf{L} \mathbf{R})^{-1} \mathbf{f} = \mathbf{A}_0^{-1} \mathbf{f} - \mathbf{A}_0^{-1} \mathbf{L} (\mathbf{I} + \mathbf{R} \mathbf{A}_0^{-1} \mathbf{L})^{-1} \mathbf{R} \mathbf{A}_0^{-1} \mathbf{f},$$

where $\mathbf{A}_0^{-1} \mathbf{L}$ can be computed once and reused for all α , and $\mathbf{A}_0^{-1} \mathbf{f}$ is evaluated once per α .

4.1. Creating the low-rank factorization of \mathbf{A}_{-1} . For simplicity of presentation, we present the technique for creating the low-rank factorization of \mathbf{A}_{-1} . We choose to create the low-rank factorization using the interpolatory decomposition [15, 9] defined as follows.

Definition 4.1. The *interpolatory decomposition* of a $m \times n$ matrix \mathbf{M} that has rank l is the factorization

$$\mathbf{M} = \mathbf{P}\mathbf{M}(J(1:l), :)$$

where J is a vector of integers j such $1 \leq j \leq m$, and \mathbf{P} is a $m \times l$ matrix that contains a $l \times l$ identity matrix. Namely, $\mathbf{P}(J(1:l), :) = \mathbf{I}_l$.

The l rows of the matrix \mathbf{M} that are picked via the interpolatory decomposition are called the *skeleton rows*. When \mathbf{M} results from the discretization of an integral equation, the row corresponds to discretization points that are called the *skeleton nodes*.

Creating the low-rank factorization of $\mathbf{A}_{-1} \in \mathbb{C}^{N \times N}$ has a computational cost that scales $O(N^2l)$ where l is the numerical rank of \mathbf{A}_{-1} . Potential theory is useful to reduce the computational cost. Specifically, we place a collection of n_{proxy} proxy charges on a surface \mathcal{P}_{-1} some distance “far” from the Γ_0 . If the interpolatory decomposition can accurately capture the interaction of Γ_0 with \mathcal{P}_{-1} , then the interpolation matrix and skeleton can accurately capture the interaction of Γ_0 with any point left of \mathcal{P}_{-1} . Circles like the one illustrated in Figure 4.1(a) are common choice for the proxy surface. This was the choice in [43, 13, 44]. In the low frequency regime we are interested in, this choice can result in an artificially large rank. Instead set \mathcal{P}_{-1} to be a half circle as illustrated in Figure 4.1(b).

Computing the interpolatory decomposition with \mathcal{P}_{-1} is not sufficient as the interactions with Γ_{-1} that lie inside \mathcal{P}_{-1} (illustrated via the blue dots in Figure 4.1) are not captured. The points on Γ_{-1} that lie inside the proxy surface are called *near points*. Let I_{near} denote the indexing for the near points. Then the matrix $\mathbf{A}_{\text{near}} = \mathbf{A}_{-1}(:, I_{\text{near}})$ is the matrix that corresponds to the interaction of Γ_0 with the near points.

Thus to create \mathbf{L}_{-1} and \mathbf{R}_{-1} , we apply the interpolatory factorization to

$$[\mathbf{A}_{\text{near}} | \mathbf{A}_{\text{proxy}}]$$

where $\mathbf{A}_{\text{proxy}}$ is the matrix that captures interactions between Γ_0 and the proxy points on \mathcal{P}_{-1} . Let J denote the index vector that results from the interpolatory decomposition. Then $\mathbf{L}_{-1} = \mathbf{P}$ resulting from the interpolatory decomposition and $\mathbf{R}_{-1} = \mathbf{A}_{-1}(J(1:l), :)$. Figure 4.1(c) illustrates the skeleton points that result from using the compression process using a half circle proxy surface.

4.2. Corner compression. When the geometry of interest has corners such as the stair geometry illustrated in Figure 4.2(a), the density has a singularity in the corner. The discretization technique must be modified to handle the singularity. An option is to use a quadrature that is specifically designed for corner singularities [35, 34, 18]. More commonly, a panel-based quadrature is used, such as [16] or [17]. Roughly speaking, the panel-based approach places a collection of panels on the geometry so that the portions away from the corners are fully resolved. Then the panels near the corner are refined in a dyadic way toward the corner to handle the singularities. Figure 4.2(b) illustrates two levels of refinement in the corners of a staircase geometry. Although the latter refinement is easy to implement, many of the discretization points placed inside the corner are not necessary for accuracy purposes. This means that the linear system is artificially large. One option is the recursively compressed inverse preconditioning (RCIP) method [17]. Since RCIP is difficult to extend to three-dimensional problems, we chose to use the corner compression method from [14].

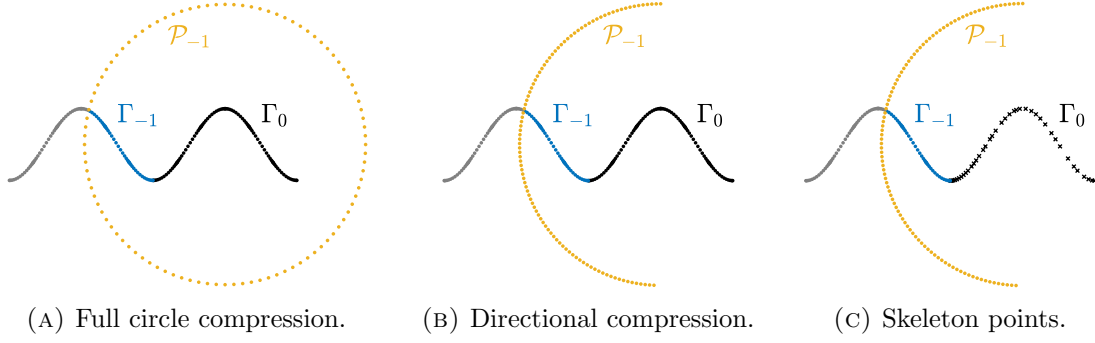


FIGURE 4.1. Illustrations of the proxy surfaces used to reduce the cost of creating the low-rank factorization of \mathbf{A}_{-1} . The unit cell boundary Γ_0 is shown in black, the near left neighbor boundary is shown in blue, and the far left neighbor boundary is shown in gray. The proxy surface \mathcal{P}_{-1} used in place of the far nodes is shown in orange. (a) The proxy surface is a full circle. (b) The proxy surface is a half circle in the direction of the neighbor boundary. (c) The skeleton points found from the interpolatory decomposition index matrix $J(1:l)$ are denoted on the unit cell boundary with black crosses.

The idea for this method is to partition the geometry according to proximity to the corner(s). Let Γ_c denote the portion of the boundary in the corner where the discretization is refined. Let Γ_s denote the remainder of the boundary. Figure 4.2(b) illustrates the boundary partitioning for a staircase geometry that has one complete corner and two half corners at the ends of the period length. Then reordering the linear system resulting from discretizing a boundary integral equation on the geometry takes the form

$$(4.5) \quad \begin{bmatrix} \mathbf{A}_{cc} & \mathbf{A}_{cs} \\ \mathbf{A}_{sc} & \mathbf{A}_{ss} \end{bmatrix} \begin{bmatrix} \mathbf{q}_c \\ \mathbf{q}_s \end{bmatrix} = \begin{bmatrix} \mathbf{f}_c \\ \mathbf{f}_s \end{bmatrix}.$$

From potential theory, we know that the interactions between Γ_c and Γ_s are low-rank. Let l denote the rank of the interactions. Then the off-diagonal blocks in the system (4.5) can be factored as follows:

$$(4.6) \quad \begin{matrix} \mathbf{A}_{cs} & = & \mathbf{U}_c & \mathbf{B}_{cs} \\ n_c \times n_s & & n_c \times l & l \times n_s \end{matrix} \quad \text{and} \quad \begin{matrix} \mathbf{A}_{sc} & = & \mathbf{B}_{sc} & \mathbf{V}_c^* \\ n_s \times n_c & & n_s \times l & l \times n_c \end{matrix}$$

When (4.6) holds, one can solve the following linear system instead of (4.5).

$$(4.7) \quad \begin{bmatrix} \mathbf{D}_{cc} & \mathbf{B}_{cs} \\ \mathbf{B}_{sc} & \mathbf{A}_{ss} \end{bmatrix} \begin{bmatrix} \tilde{\mathbf{q}}_c \\ \mathbf{q}_s \end{bmatrix} = \begin{bmatrix} \tilde{\mathbf{f}}_c \\ \mathbf{f}_s \end{bmatrix},$$

where

$$(4.8) \quad \mathbf{D}_{cc} = (\mathbf{V}_c^* \mathbf{A}_{cc}^{-1} \mathbf{U}_c)^{-1}, \quad \tilde{\mathbf{q}}_c = \mathbf{V}_c^* \mathbf{q}_c \quad \tilde{\mathbf{f}}_c = \mathbf{D}_{cc} \mathbf{V}_c^* \mathbf{A}_{cc}^{-1} \mathbf{f}_c.$$

The solution $\{\mathbf{q}_c, \mathbf{q}_s\}$ of the larger system (4.5) can be obtained from the solution $\{\tilde{\mathbf{q}}_c, \mathbf{q}_s\}$ of the smaller system (4.7) via the formula

$$(4.9) \quad \mathbf{q}_c = \mathbf{A}_{cc}^{-1} \mathbf{U}_c \mathbf{D}_{cc} \tilde{\mathbf{q}}_c + (\mathbf{A}_{cc}^{-1} - \mathbf{A}_{cc}^{-1} \mathbf{U}_c \mathbf{D}_{cc} \mathbf{V}_c^* \mathbf{A}_{cc}^{-1}) \mathbf{f}_c.$$

The equivalence holds whenever the inverses in (4.8) exist. This method can be used to reduce the computational cost of inverting \mathbf{A}_0 in the block system solver.

Remark 4.1. When \mathbf{f}_c is in the range of \mathbf{A}_{cs} it is possible to reduce [14] equation (4.9) to

$$\mathbf{q}_c = \mathbf{A}_{cc}^{-1} \mathbf{U}_c \mathbf{D}_{cc} \tilde{\mathbf{q}}_c.$$

Inverting A_{cc} is not expensive. For the stair geometry, A_{cc} is a block tridiagonal matrix where each diagonal block is the size of the number of discretization points in that corner. The diagonal blocks can be inverted independently.

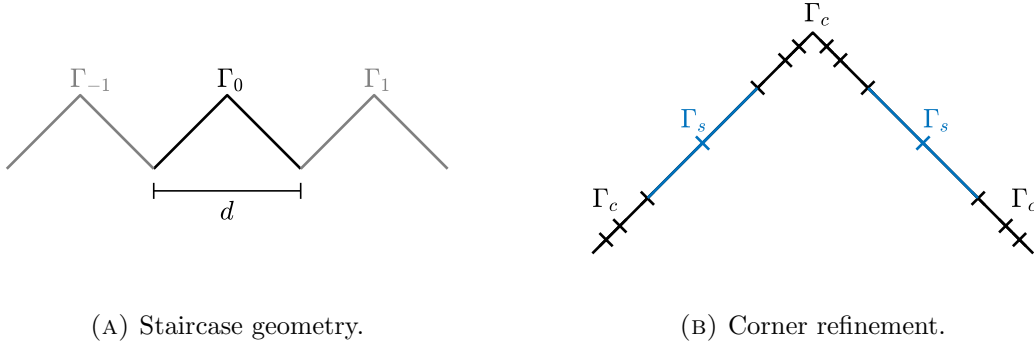


FIGURE 4.2. (a) Illustration of the partitioning of the staircase geometry with three periods. (b) Illustration of Γ_0 with the corner partitioning. Γ_c in black denotes the part of the geometry near the corner that needs refinement, $\Gamma_s = \Gamma_0 \setminus \Gamma_c$ in blue. Shown are two levels of refinement into the corner.

4.2.1. *A technique for compressing multiple corners.* To compress multiple corners, we again utilize the interpolatory decomposition and proxy surfaces. Following the procedure from Section 4.1, each corner is given a proxy circle and has a corresponding near portion as illustrated in Figure 4.3. Then a low-rank factorization via the interpolatory decomposition is found for each corner. The zoomed box in Figure 4.3 illustrates the skeleton points in the top corner. Let P_l , P_t and P_r denote the interpolation matrices for left, top and right corners respectively when creating the compressed factorization for the A_{cs} matrix. B_l , B_t and B_r are the corresponding submatrices of the original matrix containing the rows picked by the interpolatory decomposition.

Then the matrix U_c is given by

$$U_c = \begin{bmatrix} P_l & 0 & 0 \\ 0 & P_t & 0 \\ 0 & 0 & P_r \end{bmatrix}$$

and

$$B_{cs} = \begin{bmatrix} B_l \\ B_t \\ B_r \end{bmatrix}.$$

The factorization of A_{sc} is created via a similar procedure taking into account that this matrix is in the transposed location.

5. NUMERICAL RESULTS

This section reports on the performance of the proposed solution technique. For two dimensional problems, we expect the bulk of the computational gain to come from the choice of periodization method and the ability to reuse precomputed operators for all of the solves.

We chose to illustrate the performance of the method for two geometries: the cosine geometry shown in Figure 3.1 and the stair geometry shown in Figure 4.2. The period of these geometries is $d = 1$. The boundaries are discretized via composite 16-node Generalized

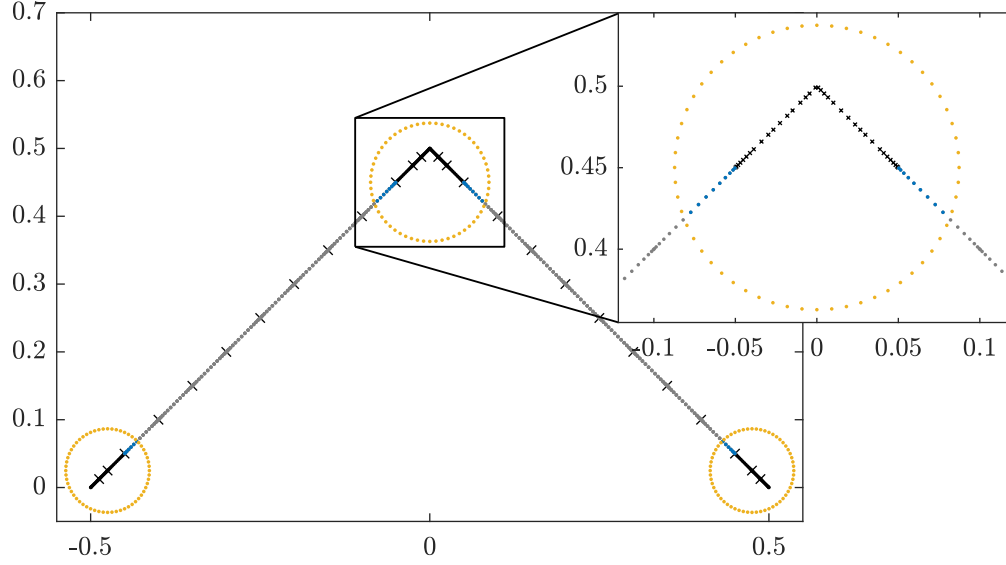


FIGURE 4.3. Illustration of a staircase geometry where the corners have two levels of refinement. The refined panels at each corner are shown in black. The near part of the remaining boundary is shown in blue, and the far part in gray. The proxy surfaces used for compression of each corner are shown in orange. The inset shows the top corner compression. The black crosses denote the skeleton points.

ALGORITHM 2: Precomputation for the quasiperiodic solver

Given two-dimensional periodic boundary Γ and wave number ω , precompute all the Bloch-phase independent portions of the solver.

Compute all the unscaled matrices in B , C , Q , Z , and V .

Compute A_0 and A_0^{-1} .

Create the low rank factors $A_{-1} \approx L_{-1}R_{-1}$ and $A_1 \approx L_1R_1$ via the technique in Section 4.1.

With these factors, create the matrix $L = [L_{-1} \ L_1]$.

Compute $A_0^{-1}L$.

For geometries with corners:

Remove the create A_0 and A_0^{-1} .

Instead, create the interpolatory decomposition for the corners via the technique in Section 4.2.1 and build all operators needed for the linear system (4.7).

Invert (4.7) directly.

Compute A_{cc}^{-1} , $A_{cc}^{-1}U_c$, D_{cc} , and $D_{cc}V_c^*$.

Use (4.9) to apply A_0^{-1} .

Gaussian quadrature [21, 16]. For the cosine geometry, the number of panels per period is N_{pan} . For the stair geometry, $0.5N_{\text{pan}}$ panels are placed on each segment of the stair case. The panel closest to each of the corners is refined dyadically with N_{ref} refinements. This

ALGORITHM 3: Application of the quasiperiodic solver

Given the operators created via Algorithm 1, a value κ , location of point charge \mathbf{x}_0 , and boundary data f_n computed via Section 3.4, solve for $\boldsymbol{\sigma}$, \mathbf{c} , and \mathbf{a} via (4.1). Then u_κ can be evaluated at $\mathbf{x} = (x, y)$ via (3.2) if $y \leq y_U$ and via (3.4) if $y > y_U$.

Appropriately scale matrices with α to create \mathbf{R} , \mathbf{B} , \mathbf{C} ,
 \mathbf{Q} , \mathbf{Z} , and \mathbf{V} .

Evaluate \mathbf{W} .

Evaluate $\mathbf{A}^{-1}\mathbf{B}$ and $\mathbf{A}^{-1}\mathbf{g}$ using the Woodbury formula (4.4).

Evaluate the Schur complement \mathbf{S} defined in (4.2).

Create the SVD of \mathbf{S} .

Evaluate $\mathbf{b} = \mathbf{S}^\dagger(\hat{\mathbf{C}}\mathbf{A}^{-1}\mathbf{g})$ using the SVD to apply \mathbf{S}^\dagger .

Evaluate $\boldsymbol{\sigma} = \mathbf{A}^{-1}\mathbf{g} - \mathbf{A}^{-1}\hat{\mathbf{B}}\mathbf{b}$ using the already computed $\mathbf{A}^{-1}\mathbf{B}$.

means that the total number of panels on the stair case geometry is then $N_{\text{pan}} + 4N_{\text{ref}}$. For all experiments, N denotes the total number of discretization points on the boundary in the unit cell and the compression tolerance ϵ is set to 10^{-13} .

The walls of the unit cell are set to be 1 unit in height. The number of Legendre-Gauss nodes for the left and right walls is set to $M_w = 240$, so there are 120 nodes on each wall. The number of equispaced nodes on the top wall is set to $M = 60$. The truncation of the Rayleigh-Bloch expansion is set to $K = 20$. The proxy circle \mathcal{P} is set to have $N_{\text{proxy}} = 160$ equispaced points. The radius of the proxy circle is $R_{\text{proxy}} = 2d$.

For any interpolatory decomposition calculations, the number of points on the proxy surface is set to $n_{\text{proxy}} = 100$. These proxy circles or half circles are concentric to the geometry segment of interest with a radius scaled by 1.75.

For the examples under consideration here, we take the source point to be $\mathbf{x}_0 = (-0.2, 0.35)$ and the point where we wish to evaluate the solution to be $\mathbf{x} = (0.3, 0.25)$.

All results were computed on a Dell Precision 7920 Tower, with two 12-core Intel Xeon Gold 6128 processors and 192 GB of memory. The algorithm was implemented in Matlab.

The numerical examples first illustrate the performance of the direct solution technique allowing for the cost for the precomputation and the application of the solver to be easily observed. Then the solver is used to approximate the Floquet–Bloch integral (1.4) and a comparison with the quasiperiodic Green’s function approach from [1] as implemented in [2] is conducted.

5.1. Performance of the direct solver. To illustrate the performance of the direct solution technique we consider solving (1.5) with $\omega = 1.2$ and $\theta = \pi/5$. Recall $\kappa = \omega \cos \theta$ and $\alpha = e^{i\kappa d}$. For each experiment the relative error is computed by comparing with the solution generated with the largest number of panels.

5.1.1. The direct solver: cosine geometry. To illustrate the benefit of low rank linear algebra, we consider three different approaches to building the direct solver for the cosine geometry. For each approach, the α –independent blocks are precomputed but the calculation of \mathbf{A}^{-1} differs. The three different approaches are:

- **Dense:** The matrix \mathbf{A}^{-1} is inverted directly in the solve.

- **ID proxy:** The precomputation includes the low-rank factorizations for A_{-1} and A_1 using a full proxy circle (see Figure 4.1(a)), evaluating A_0^{-1} , and evaluating $A_0^{-1}L$. The Woodbury formula is used to apply A^{-1} in the solve.
- **Half circle:** The precomputation includes the low-rank factorizations for A_{-1} and A_1 using a half proxy circle (see Figure 4.1(b)), evaluating A_0^{-1} and evaluating $A_0^{-1}L$. The Woodbury formula is used to apply A^{-1} in the solve.

Table 1 reports the time in seconds and the relative error for using the different direct solver options for the cosine geometry with various number of panels. While building the low rank factorizations makes the precomputation portion of the solver slower, the speed of applying the solver with the factorizations is much faster. In this example, the factorization solver will be faster than the dense linear algebra solver any time the integral (1.4) requires more than 3 solves.

Cosine Geometry	N_{pan}	4	8	20	40	100	200
	N	64	128	320	640	1600	3200
Precomp Time	Dense	0.095	0.16	0.38	0.75	2.35	5.93
	ID proxy	0.11	0.21	0.47	0.87	2.48	7.03
	Half circle	0.10	0.17	0.42	0.77	2.27	6.35
Solve Time	Dense	0.018	0.021	0.023	0.034	0.16	0.58
	ID proxy	0.022	0.022	0.023	0.025	0.042	0.083
	Half circle	0.020	0.019	0.022	0.026	0.040	0.069
Error	Dense	1.1e-10	1.0e-13	8.6e-14	8.1e-14	1.3e-13	
	ID proxy	1.2e-10	9.9e-14	8.4e-14	5.0e-14	1.2e-13	
	Half circle	1.1e-10	1.0e-13	1.7e-13	2.7e-13	2.3e-13	

TABLE 1. Time in seconds for the precomputation and solve stages of the direct solver applied to the cosine geometry. The relative error is also reported.

5.1.2. *The direct solver: stair geometry.* The performance of the direct solver on a geometry with corners is illustrated in this section. For these experiments 8 uniform panels are placed on each of the straight edges, i.e. $N_{\text{pan}} = 16$. This choice results in an approximation that is accurate to four digits. Additional dyadic spaced panels are placed in each corner to gain additional accuracy. The number of refinements N_{ref} range from 0 to 36. In these experiments, we compare the Dense and ID proxy half circle and Corner compression precomputation options. The Corner compression option is described here.

Corner compression: The precomputation includes the low-rank factorizations for A_{-1} and A_1 using a half proxy circle (see Figure 4.1(b)), the corner compression for constructing the action of A_0 and the matrix $A_0^{-1}L$. The Woodbury formula is used to apply A^{-1} in the solve.

Table 2 reports the times for the precomputation and solve stages of the direct solvers. The slight increase in the time to apply the solver for the ID proxy half circle solver is the result of slightly higher ranks in the neighbor interaction matrices A_{-1} and A_1 . The corner compression method has the fastest time for applying the direct solver. It would take seven solves for the corner compression method to be faster than using the dense linear algebra solver.

Table 3 reports the size of the corner compressed system for the different number of refinements. While the size of D_{cc} remains fixed for levels of refinement, the accuracy of the approximation is improved. This illustrates that the low rank factorization is doing a good job picking the “important” discretization points as skeleton points. It is also important to note that while over 2000 points are used in the discretization to get 8 digits of accuracy, the

Stair Geometry	N_{ref}	0	6	12	24	36
	N	256	640	1024	1792	2560
Precomp Time	Dense	0.31	0.74	1.27	2.86	6.08
	Half circle	0.35	0.82	1.25	2.82	5.32
	Corner compression	0.40	0.96	1.68	3.04	5.87
Solve Time	Dense	0.022	0.033	0.059	0.19	0.36
	Half circle	0.020	0.025	0.034	0.048	0.079
	Corner compression	0.023	0.027	0.035	0.055	0.080
Error	Dense	2.9e-04	1.5e-05	9.8e-07	3.9e-09	
	Half circle	2.7e-04	1.6e-05	1.0e-06	3.8e-09	
	Corner compression	2.5e-04	1.5e-05	9.3e-07	3.9e-09	

TABLE 2. Time in seconds for the precomputation and solve stages of the direct solver applied to the stair geometry with N_{ref} refinements into each corner. The relative error is also reported.

N_{ref}	N	N_{compress}
0	256	256
6	640	292
12	1014	292
24	1702	292
36	2560	292

TABLE 3. The number of refinements into the corners N_{ref} , the total number of points on the stair N , and the size of compressed system N_{compress} when corner compression is used on the stair geometry.

5.2. Performance of the full solution technique. If the full solution to the aperiodic problem is desired, we need to evaluate the Floquet–Bloch integral (1.4) using the technique for constructing quadrature points and weights outlined in Section 2. This section illustrates the performance of the solution technique for evaluating that integral with three different choices of wave number: $\omega = 1.2$, $\omega = 2.4$, and $\omega = 0.01$. For these experiments, we label the results from the method [1, 2] as **QP approach**. Any dashed entries in the tables correspond to experiments that we were not able to conduct due to memory constraints.

5.2.1. *Away from the branch points.* When $\omega = 1.2$ the contour for the Floquet–Bloch transform (2.2) is away from the branch points and no refinement is needed to obtain high accuracy. Thus it is enough to use trapezoidal rule on the contour. We set $N_\kappa = 60$. This means that 60 quasiperiodic boundary value solves are required to evaluate u .

First, we consider the cosine geometry. Figure 5.1(a) illustrates the relative error for the solution due to a point source for different numbers of panels. The solution technique is able to achieve 13 digits of accuracy with roughly 10 panels (i.e. 160 points) on the boundary. Table 4 reports the time in seconds required to evaluate the approximation. The more points there are on the geometry, the more benefit there is to using the low rank versions of the solver.

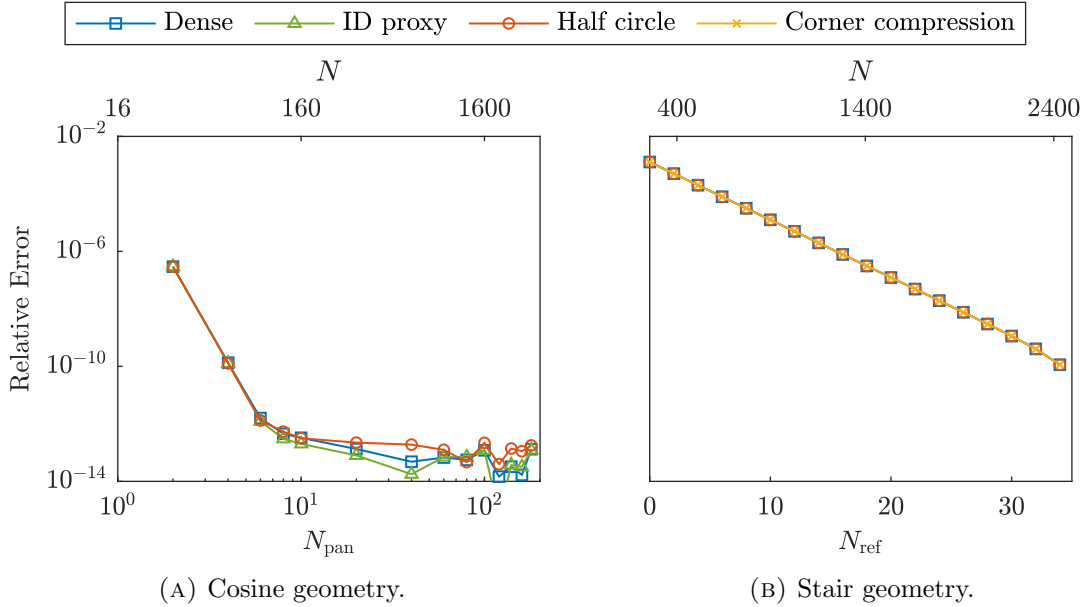


FIGURE 5.1. (a) Number of panels N_{pan} versus the relative error for evaluating the Floquet–Bloch integral for the cosine geometry. (b) Number of refinements N_{ref} versus the relative error for evaluating the Floquet–Bloch integral for the stair geometry.

Cosine Geometry						
N_{pan}	4	8	20	40	100	200
N	64	128	320	640	1600	3200
QP approach	2.4	4.5	13	35	179	–
Dense	2.7	3.0	3.9	5.6	16	52
ID proxy	2.8	3.3	4.4	6.2	13	23
Half circle	2.7	3.1	4.0	5.8	11	20

TABLE 4. The time in seconds for evaluating the Floquet–Bloch integral (1.4) with the cosine geometry, $\omega = 1.2$ and $N_\kappa = 60$ Floquet–Bloch nodes for the QP approach, Dense, ID proxy and Half circle solvers.

Next, we consider the stair geometry. Figure 5.1(b) illustrates the relative error for the solution due to a point source. Table 5 reports the time in seconds required to evaluate the approximation. In this example, the refinements are necessary to gain accuracy and using the low rank linear algebra is roughly twice as fast as using dense linear algebra. The proposed method is roughly 20 times faster than the QP approach for this problem when 9 digits of accuracy are desired.

Stair Geometry					
N_{ref}	0	6	12	24	36
N	256	640	1024	1792	2560
QP approach	11	38	80	235	539
Dense	3.8	6.3	9.0	22	36
Half circle	3.9	5.6	7.7	14	20
Corner compression	4.2	6.4	8.5	13	19

TABLE 5. The time in seconds for evaluating the Floquet–Bloch integral (1.4) with the stair geometry, $\omega = 1.2$ and $N_{\kappa} = 60$ Floquet–Bloch nodes for the QP approach, Dense, Half circle, and Corner compression solvers.

5.2.2. *Near the branch points.* When $\omega = 2.4$ and $\omega = 0.01$, the contour (2.2) passes between two coalescing branch points and the refinement procedure defined in equation (2.3) is necessary. For these experiments, the exponential grating parameter b is set to 5.

For the cosine geometry, the number of panels is fixed to $N_{\text{pan}} = 10$. Table 6 shows the timing and error results of the full solution evaluation for various N_{κ} nodes. Since many points are not required to resolve the geometry, the improvement from the proposed technique is small. This was expected from the previous sections results.

Cosine geometry		$\omega = 2.4$			$\omega = 0.01$		
	N_{κ}	40	60	150	60	120	150
Time	QP approach	5.77	6.26	15.0	4.89	8.41	10.3
	Half circle	2.56	3.40	9.12	3.21	6.16	7.56
Error	QP approach	3.7e-05	9.6e-08		2.7e-05	7.2e-09	
	Half circle	3.6e-05	9.5e-08		5.7e-05	9.6e-09	

TABLE 6. The time in seconds for evaluating the Floquet–Bloch integral (1.4) with the cosine geometry, $\omega = 2.4$ and $\omega = 0.01$ for the QP approach and Half circle solvers. The relative error is also reported.

For the stair geometry, the number of panels and number of refinements are fixed. Specifically, $N_{\text{pan}} = 16$ and $N_{\text{ref}} = 30$. Table 7 gives timing and error results of the full solution evaluation for various N_{κ} nodes. For $\omega = 2.4$, the number of quadrature nodes needed on the contour (2.3) to achieve an 11 digit accurate approximation is $N_{\kappa} = 60$. When $\omega = 0.01$, the contour is closer to the branch points. This means that additional refinement is needed to gain accuracy. In this experiment, $N_{\kappa} = 120$ quadrature nodes were needed to obtain an approximation that is accurate to 8 digits. Table 7 reports the timings for both the QP approach and the Corner compression approach. Since the case of $\omega = 0.01$

require many solves to achieve high accuracy, there is a 33 times speed up using the Corner compression method instead of the QP approach.

Stair geometry		$\omega = 2.4$			$\omega = 0.01$		
	N_κ	40	60	150	60	120	150
Time	QP approach	122	504	1376	337	637	814
	Corner compression	13	15	32	11	19	23
Error	QP approach	1.8e-07	7.5e-11		2.8e-05	7.6e-09	
	Corner compression	1.7e-07	7.0e-11		6.0e-05	1.7e-08	

TABLE 7. The time in seconds for evaluating the Floquet–Bloch integral (1.4) with the stair geometry, $\omega = 2.4$ and $\omega = 0.01$ for the QP approach and Corner compression solvers. The relative error is also reported.

6. CONCLUDING REMARKS

This manuscript presents an efficient direct solution technique for quasiperiodic scattering problems where the geometry does not require many discretization points to get high accuracy. The technique utilizes many of the ideas from traditional fast direct solvers to create problem scale appropriate acceleration. The benefit of the solution technique is observed when approximating the Floquet–Bloch integral which requires many solves. For the problems in this paper, proposed solution technique observes 20-30 times speed up for evaluating the Floquet–Bloch integral for a geometry with corners when compared with a solution technique based on the quasiperiodic Green’s function.

For practical purposes, most users would benefit from simply utilizing the proposed periodizing scheme (Section 3) and precomputation with dense matrices. This is because the geometry has to be complicated enough to justify a large number of discretization points on order for the low rank linear algebra to be useful. For three-dimensional problems, the number of discretization points will be larger and the quasiperiodic Green’s function will be just as expensive (possibly more expensive) to evaluate. This means that the low rank linear algebra technique has the potential to see more benefits for these problems. This is being investigated by the authors.

7. ACKNOWLEDGEMENTS

The work by A. Gillman is supported by the National Science Foundation (DMS-2110886), and a Knut and Alice Wallenberg Foundation Grant. A. Gillman conducted a portion of this work while visiting the Institut Mittag-Leffler.

REFERENCES

- [1] F. J. Agoes and A. H. Barnett. Trapped acoustic waves and raindrops: high-order accurate integral equation method for localized excitation of a periodic staircase. *Journal of Computational Physics*, 519:113383, 2024.
- [2] F. J. Agoes, T. Goodwill, and J. Hoskins. Complex scaling for the junction of semi-infinite gratings, 2025.
- [3] T. Arens, N. Shafieeabyaneh, and R. Zhang. A high-order numerical method for solving non-periodic scattering problems in three-dimensional bi-periodic structures. *ZAMM-Journal of Applied Mathematics and Mechanics/Zeitschrift für Angewandte Mathematik und Mechanik*, 104(9):e202300650, 2024.
- [4] A. Barnett and L. Greengard. A new integral representation for quasi-periodic fields and its application to two-dimensional band structure calculations. *Journal of Computational Physics*, 229(19):6898–6914, 2010.

- [5] A. H. Barnett, G. R. Marple, S. Veerapaneni, and L. Zhao. A unified integral equation scheme for doubly periodic laplace and stokes boundary value problems in two dimensions. *Communications on Pure and Applied Mathematics*, 71(11):2334–2380, 2018.
- [6] A.-S. Bonnet-Bendhia and F. Starling. Guided waves by electromagnetic gratings and non-uniqueness examples for the diffraction problem. *Mathematical Methods in the Applied Sciences*, 17(5):305–338, 1994.
- [7] O. P. Bruno and M. C. Haslam. Efficient high-order evaluation of scattering by periodic surfaces: deep gratings, high frequencies, and glancing incidences. *Journal of the Optical Society of America A*, 26(3):658–668, 2009.
- [8] F. Capolino, D. R. Jackson, and D. R. Wilton. Mode excitation from sources in two-dimensional EBG waveguides using the array scanning method. *IEEE Microwave and Wireless Components Letters*, 15(2):49–51, 2005.
- [9] H. Cheng, Z. Gimbutas, P. Martinsson, and V. Rokhlin. On the compression of low rank matrices. *SIAM Journal of Scientific Computing*, 26:1389–1404, 2005.
- [10] M. Cho and A. Barnett. Robust fast direct integral equation solver for quasi-periodic scattering problems with a large number of layers. *Optics Express*, 23:1775–1799, 2015.
- [11] P. J. Cobelli, V. Pagneux, A. Maurel, and P. Petitjeans. Experimental study on water-wave trapped modes. *Journal of Fluid Mechanics*, 666:445–476, 2011.
- [12] J. DeSanto, G. Erdmann, W. Hereman, and M. Misra. Theoretical and computational aspects of scattering from rough surfaces: one-dimensional perfectly reflecting surfaces. *Waves in Random Media*, 8(4):385, 1998.
- [13] A. Gillman and A. Barnett. A fast direct solver for quasiperiodic scattering problems. *Journal of Computational Physics*, pages 309–322, 2013.
- [14] A. Gillman, S. Hao, and P. Martinsson. A simplified technique for the efficient and highly accurate discretization of boundary integral equations in 2D on domains with corners. *Journal of Computational Physics*, 256:214–219, 2014.
- [15] M. Gu and S. C. Eisenstat. Efficient algorithms for computing a strong rank-revealing QR factorization. *SIAM Journal on Scientific Computing*, 17:848–869, 1996.
- [16] S. Hao, A. H. Barnett, P.-G. Martinsson, and P. Young. High-order accurate methods for Nyström discretization of integral equations on smooth curves in the plane. *Advances in Computational Mathematics*, 40(1):245–272, 2014.
- [17] J. Helsing and R. Ojala. Corner singularities for elliptic problems: integral equations, graded meshes, quadrature, and compressed inverse preconditioning. *Journal of Computational Physics*, 227:8820–8840, 2008.
- [18] J. G. Hoskins, V. Rokhlin, and K. Serkh. On the numerical solution of elliptic partial differential equations on polygonal domains. *SIAM Journal on Scientific Computing*, 41(4):A2552–A2578, 2019.
- [19] H. Kagemoto. Minimization of wave forces on an array of floating bodies — the inverse hydrodynamic interaction theory. *Applied Ocean Research*, 14(2):83–92, 1992.
- [20] A. Khelif, A. Choujaa, B. Djafari-Rouhani, M. Wilm, S. Ballandras, and V. Laude. Trapping and guiding of acoustic waves by defect modes in a full-band-gap ultrasonic crystal. *Phys. Rev. B*, 68:214301, Dec 2003.
- [21] P. Kolm and V. Rokhlin. Numerical quadratures for singular and hypersingular integrals. *Computers & Mathematics with Applications*, 41(3):327–352, 2001.
- [22] A. Kress and G. F. Roach. Transmission problems for the Helmholtz equation. *Journal of Mathematical Physics*, 19:1433–1437, 1978.
- [23] A. Lechleiter and R. Zhang. Non-periodic acoustic and electromagnetic, scattering from periodic structures in 3D. *Computers & Mathematics with Applications*, 74(11):2723–2738, 2017.
- [24] Y. Li, X. Jiang, R.-q. Li, B. Liang, X.-y. Zou, L.-l. Yin, and J.-c. Cheng. Experimental realization of full control of reflected waves with subwavelength acoustic metasurfaces. *Phys. Rev. Appl.*, 2:064002, Dec 2014.
- [25] G. Ma and P. Sheng. Acoustic metamaterials: From local resonances to broad horizons. *Science Advances*, 2(2):e1501595, 2016.
- [26] P. McIver. Wave interaction with arrays of structures. *Applied Ocean Research*, 24(3):121–126, 2002.
- [27] P. McIver, C. Linton, and M. McIver. Construction of trapped modes for wave guides and diffraction gratings. *Proceedings of the Royal Society of London. Series A: Mathematical, Physical and Engineering Sciences*, 454(1978):2593–2616, 1998.
- [28] W. Meng. A new periodic FM-BEM for solving the acoustic transmission problems in periodic media. *Engineering Analysis with Boundary Elements*, 154:54–63, 2023.

- [29] A. Moroz. Quasi-periodic Green's functions of the Helmholtz and Laplace equations. *Journal of Physics A: Mathematical and General*, 39(36):11247, 2006.
- [30] V. Pagneux. *Trapped Modes and Edge Resonances in Acoustics and Elasticity*, pages 181–223. Springer Vienna, Vienna, 2013.
- [31] J. Pinto, R. Aylwin, and C. Jerez-Hanckes. Fast solver for quasi-periodic 2D-Helmholtz scattering in layered media. *ESAIM: Mathematical Modelling and Numerical Analysis*, 55(5):2445–2472, 2021.
- [32] R. Porter and D. V. Evans. Rayleigh–Bloch surface waves along periodic gratings and their connection with trapped modes in waveguides. *Journal of Fluid Mechanics*, 386:233–258, 1999.
- [33] V. Rokhlin. Solution of acoustic scattering problems by means of second kind integral equations. *Wave Motion*, 5:257–272, 1983.
- [34] K. Serkh. On the solution of elliptic partial differential equations on regions with corners II: Detailed analysis. *Applied and Computational Harmonic Analysis*, 46(2):250–287, 2019.
- [35] K. Serkh and V. Rokhlin. On the solution of the Helmholtz equation on regions with corners. *Proceedings of the National Academy of Sciences*, 113(33):9171–9176, 2016.
- [36] L. N. Trefethen and J. A. C. Weideman. The exponentially convergent trapezoidal rule. *SIAM Review*, 56(3):385–458, 2014.
- [37] R. Wood. XLIV. A suspected case of the electrical resonance of minute metal particles for light-waves. A new type of absorption. *The London, Edinburgh, and Dublin Philosophical Magazine and Journal of Science*, 3(16):396–410, 1902.
- [38] B. Wu and M. H. Cho. Robust fast direct integral equation solver for three-dimensional doubly periodic scattering problems with a large number of layers. *Journal of Computational Physics*, 495:112573, 2023.
- [39] C. Wu and V. Galindo. Properties of a phased array of rectangular waveguides with thin walls. *IEEE Transactions on Antennas and Propagation*, 14(2):163–173, 1966.
- [40] K. Yasumoto and K. Yoshitomi. Efficient calculation of lattice sums for free-space periodic Green's function. *IEEE Transactions on Antennas and Propagation*, 47(6):1050–1055, 2002.
- [41] R. Zhang. A high order numerical method for scattering from locally perturbed periodic surfaces. *SIAM Journal on Scientific Computing*, 40(4):A2286–A2314, 2018.
- [42] R. Zhang. Numerical methods for scattering problems in periodic waveguides. *Numerische Mathematik*, 148(4):959–996, 2021.
- [43] Y. Zhang and A. Gillman. A fast direct solver for two dimensional quasi-periodic multilayered media scattering problems. *BIT Numerical Mathematics*, 61(1):141–171, 2021.
- [44] Y. Zhang and A. Gillman. A fast direct solver for two dimensional quasi-periodic multilayered media scattering problems, Part II, 2022.